Supporting Information for
Nanostructure-dependent indentation fracture toughness of metal-organic framework monoliths

Michele Tricarico and Jin-Chong Tan[*]

* Jin-Chong Tan.

Email: jin-chong.tan@eng.ox.ac.uk

Table S1. Mechanical properties of the monoliths obtained from nanoindentation with a Berkovich tip. The indentation fracture toughness was estimated by measuring the length of the radial cracks induced by nanoindentation with a cube corner tip. The values for E^* (letting $v_s = 0$) and H were computed by averaging the CSM data between 500 and 1000 nm. For the materials whose Poisson's ratio (v) is known from simulations study, also the Young's modulus was computed (see Methods). The mean and standard deviations were calculated from 32 individual indents. The residual depth at the end of the indentation test was determined from the load-depth curves (Figure S2).

Monolith Sample	Density (g/cm³)	Indentation Modulus, E^* (GPa)	Poisson's Ratio, v	Young's Modulus, E (GPa)	Hardness, H (MPa)	Elastic energy $W_{elastic}/W_{total}$ (%)	Indentation fracture toughness, K_c (MPa$\sqrt{m}$)	Residual depth – load-depth curves (nm)	Residual depth – AFM (nm)
ZIF-8 ref. [1]	1.246 ± 0.010	3.78 ± 0.44	0.43 [2]	3.18 ± 0.04	452 ± 20	64.1 ± 1.8	0.074 ± 0.023	-	-
ZIF-8 This work	1.258 ± 0.022	4.03 ± 0.03	0.43 [2]	3.28 ± 0.03	534 ± 6	65.3 ± 1.4	0.081 ± 0.011	336 ± 5	246 ± 4
HKUST-1	1.529 ± 0.043	15.25 ± 0.61	0.45 [3]	12.16 ± 0.48	761 ± 53	39.0 ± 1.8	0.80 ± 0.45	602 ± 18	200 ± 1
MIL-68	1.475 ± 0.007	13.24 ± 0.52 [4]	-	-	402 ± 13 [4]	19.2 ± 1.0	-	861 ± 5	567 ± 20
MOF-808	1.522 ± 0.104	4.61 ± 0.32	-	-	122 ± 14	13.6 ± 1.1	-	948 ± 13	538 ± 5

Sample	Scratch Critical Depth (nm)	Cross Profile Max Depth (nm)
ZIF-8 plough	3088 ± 94	580 ± 72
HKUST-1 plough	1764 ± 60	671 ± 441
MIL-68 plough	4149 ± 339	1187 ± 209
MOF-808 plough	9255 ± 573	3266 ± 452
ZIF-8 push	3002 ± 170	911 ± 288
HKUST-1 push	2379 ± 138	502 ± 106
MIL-68 push	4895 ± 49	2050 ± 152
MOF-808 push	10549 ± 467	3762 ± 581

Table S2. Results of nanoscratch tests on the monoliths in the ploughing and pushing modes.
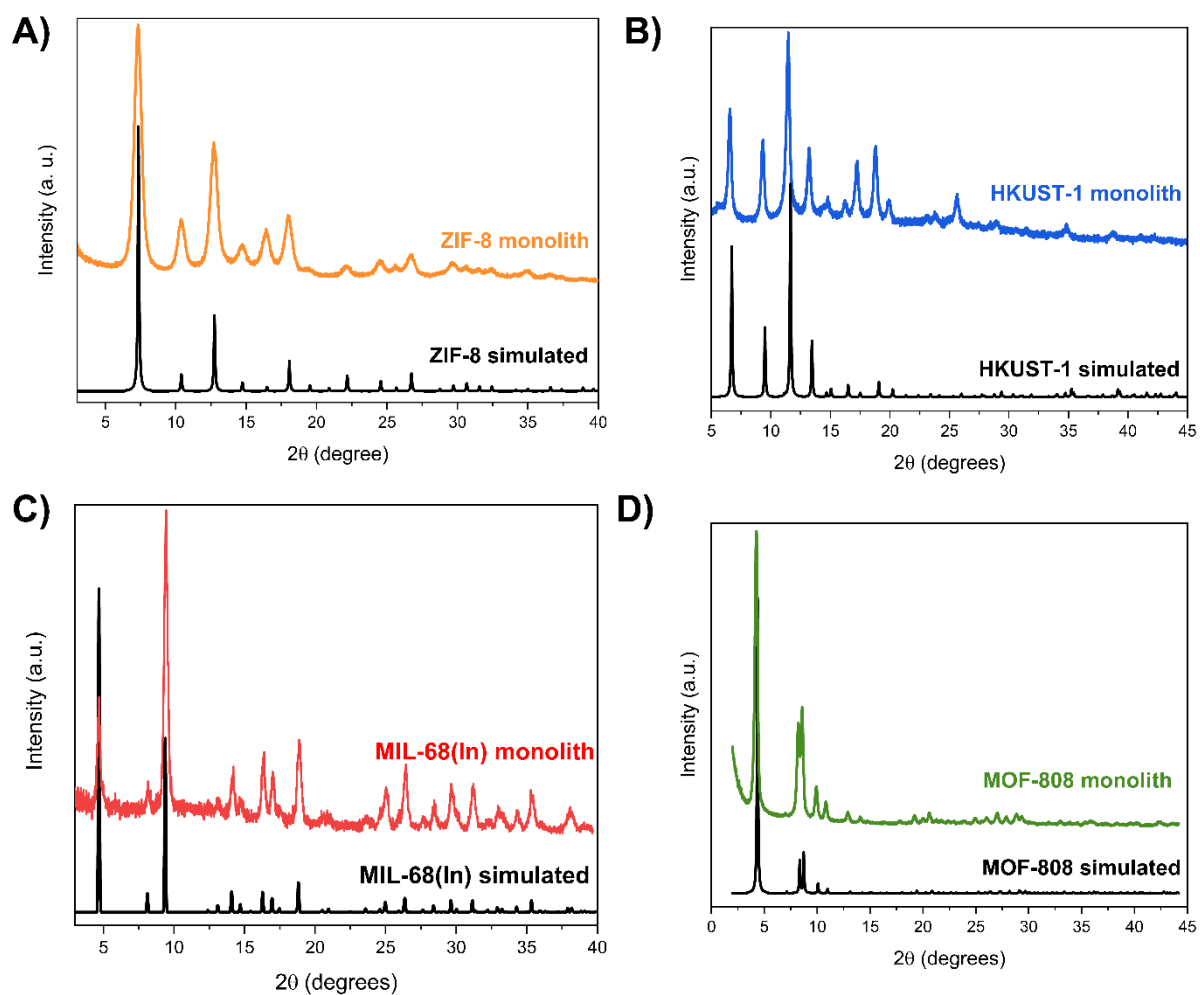
Figure S1. XRD patterns of A) ZIF-8, B) HKUST-1, C) MIL-68 and D) MOF-808 monoliths in comparison with the simulated patterns from the Cambridge Structural Database (CSD). CCDC codes: TUDKEJ (ZIF-8), FIQCEN (HKUST-1), LOQLEJ (MIL-68(In)), BOHWUS (MOF-808).
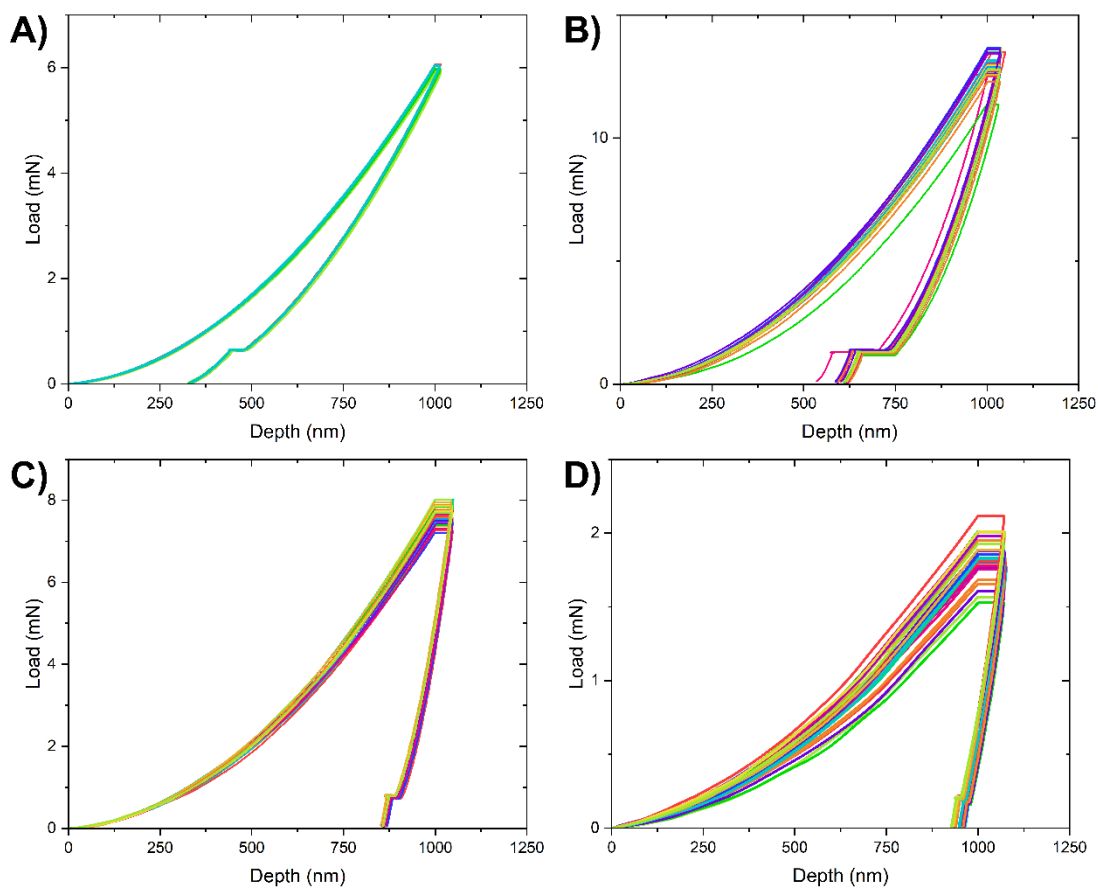
Figure S2. Nanoidentation load-depth curves with a Berkovich indenter to a maximum surface penetration depth of 1000 nm. (A) ZIF-8, (B) HKUST-1, (C) MIL-68 and (D) MOF-808. 32 indentations per sample were performed.
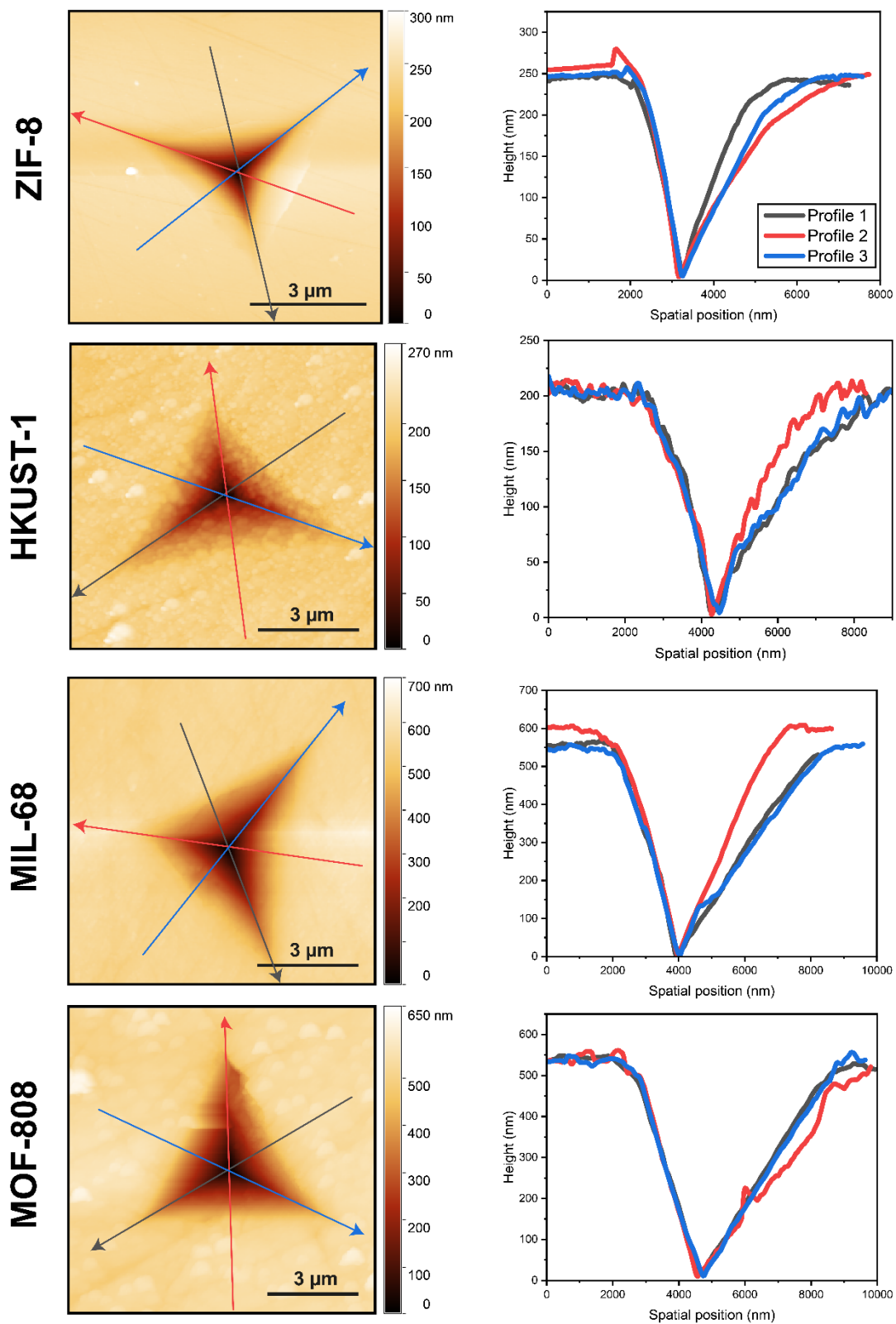
Figure S3. AFM topographies of the residual indents on the four monoliths. The corresponding cross-sectional profiles along the specified paths are plotted on the right.
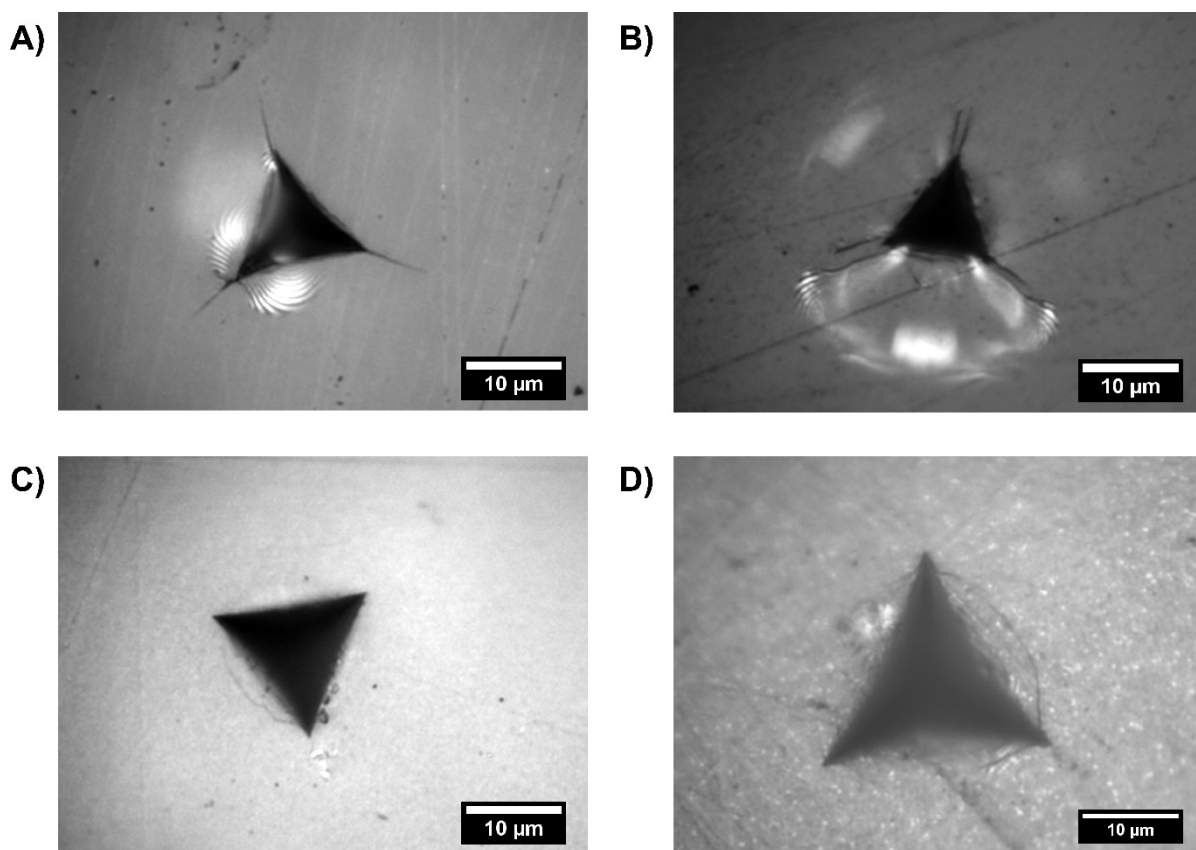
Figure S4. Cube corner residual indents on A) ZIF-8, B) HKUST-1, C) MIL-68, and D) MOF-808. A maximum load of 50 mN was applied in all tests.
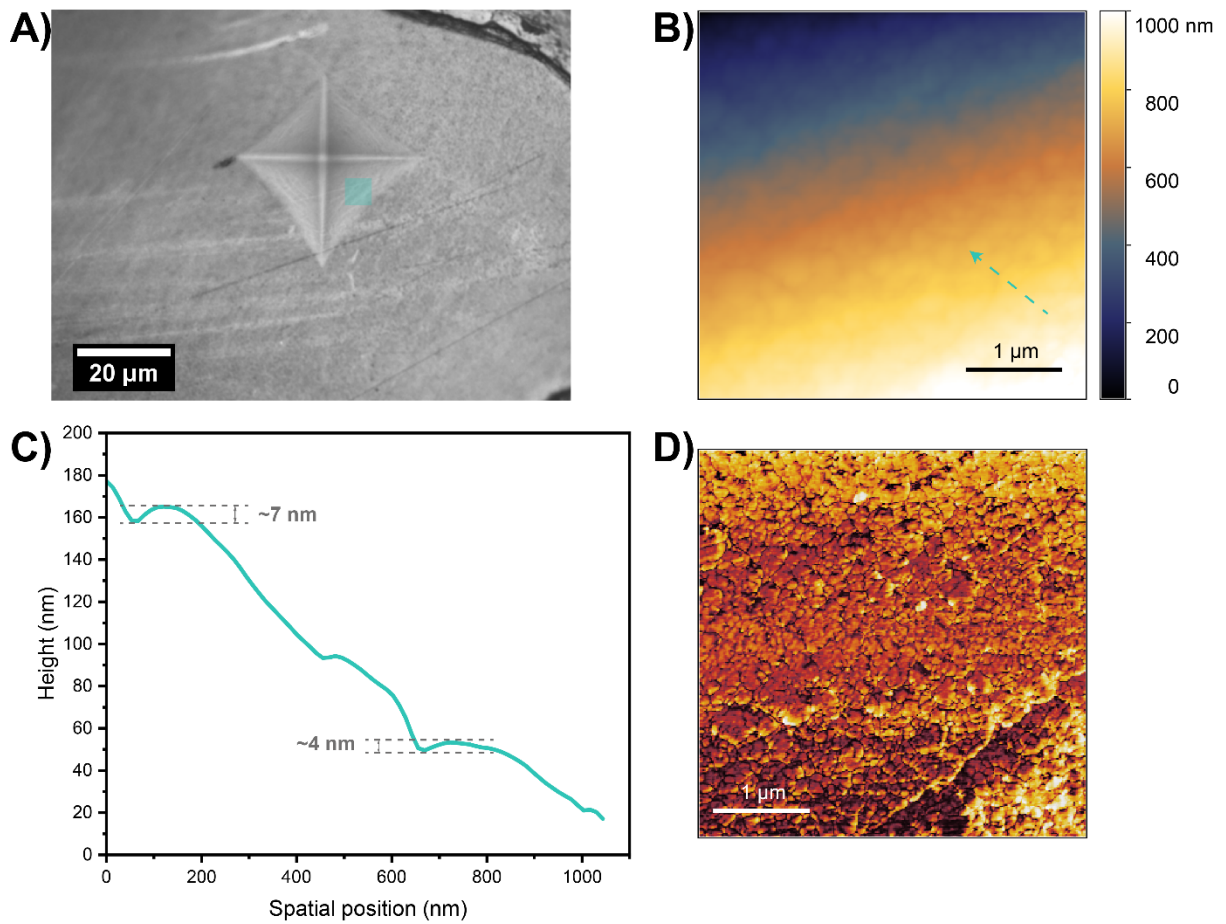
Figure S5. Detail of shear faults on a HKUST-1 monolith. A) Overview of the Vickers residual indent HV0.05 (50 gf ~ 0.49 N). B) AFM height topography of a 4×4 μm scan area, highlighted in A). C) AFM height profile along the line highlighted in B), revealing the vertical displacement corresponding to the shear faults. D) AFM phase image revealing the location of the shear fault, which was less visible from height topography alone.
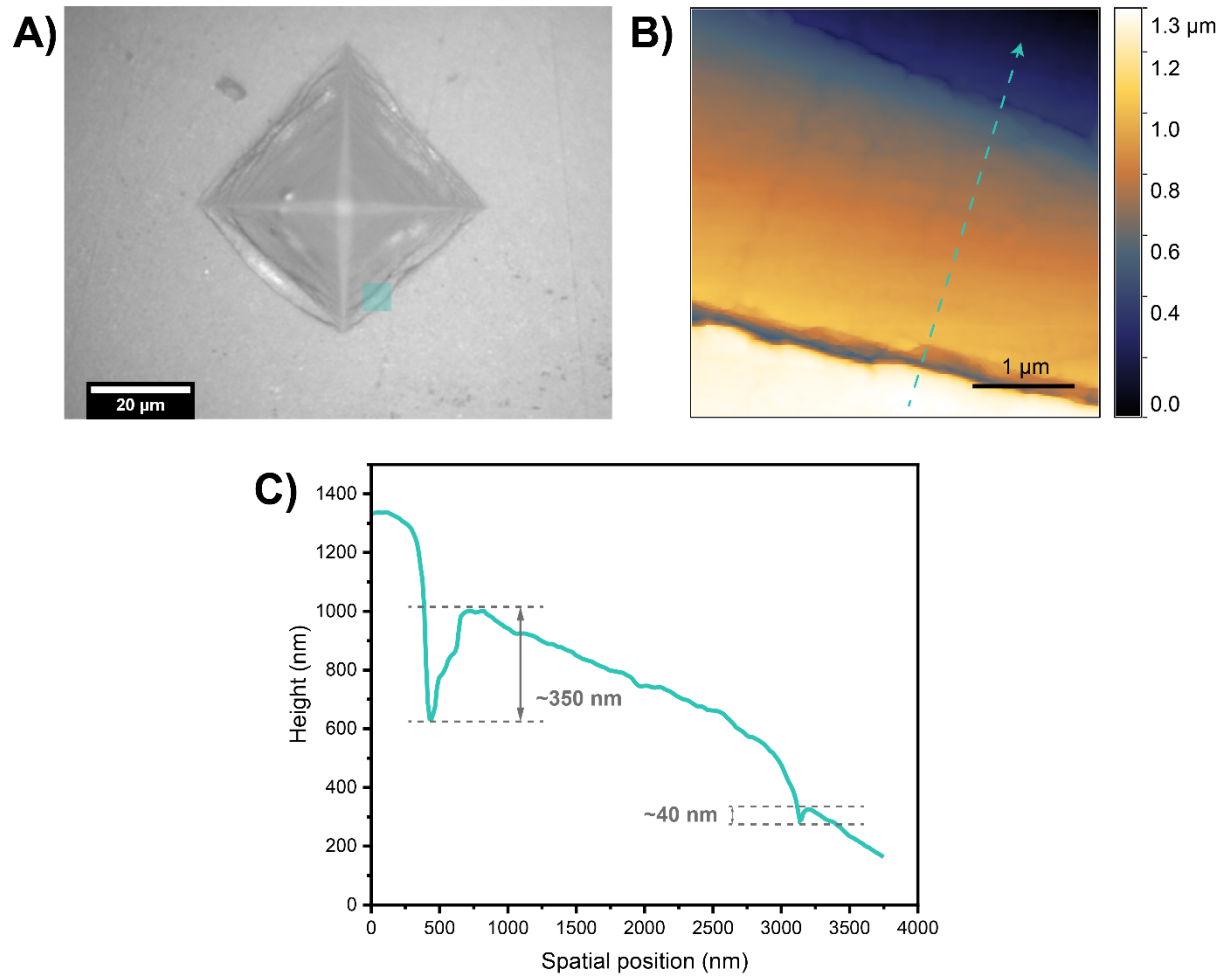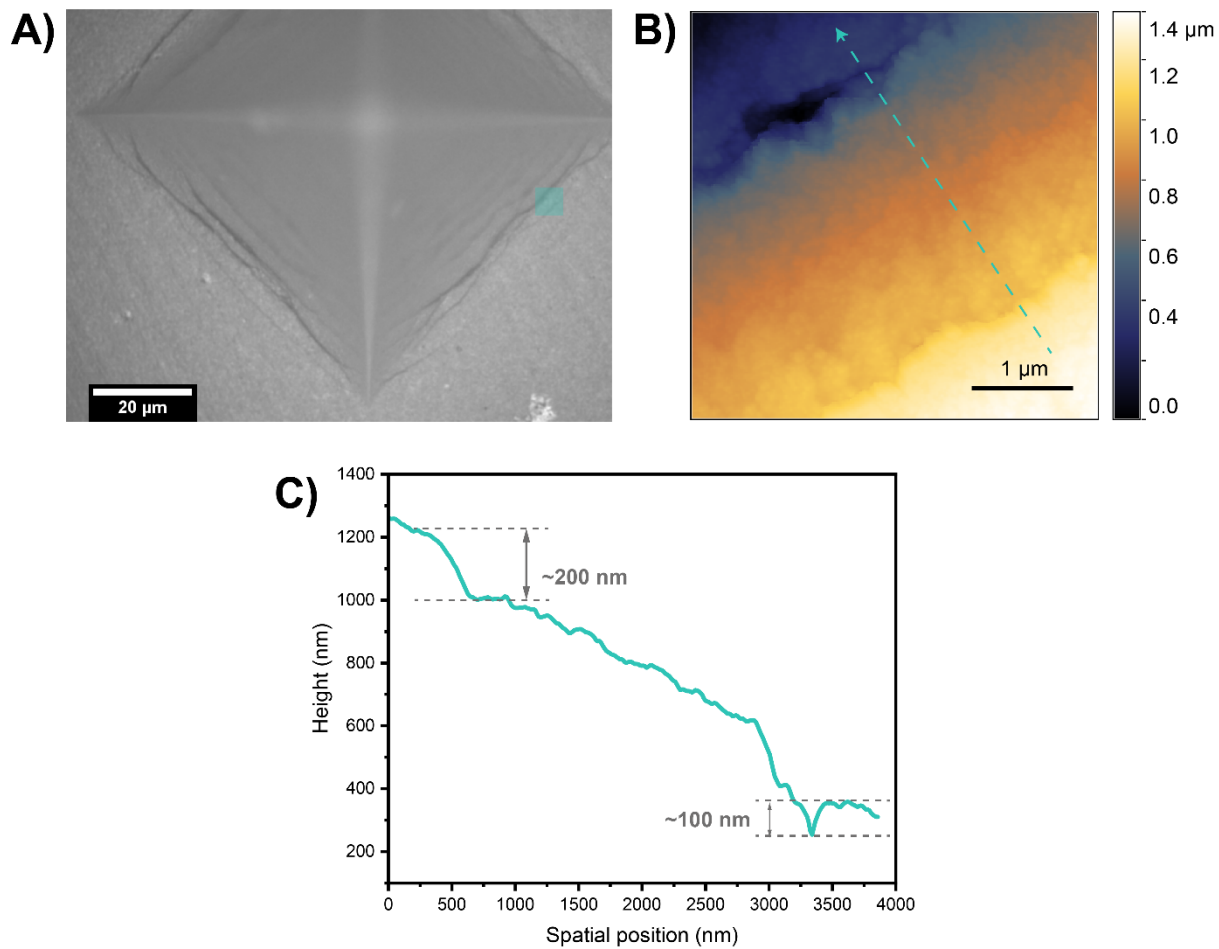
Figure S6. Detail of shear faults on a MIL-68 monolith. A) Overview of the Vickers residual indent HV0.05 (50 gf ~ 0.49 N). B) AFM height topography of a 4×4 μm scan area, highlighted in A). C) AFM height profile along the line highlighted in B), revealing the vertical displacement corresponding to the shear faults.
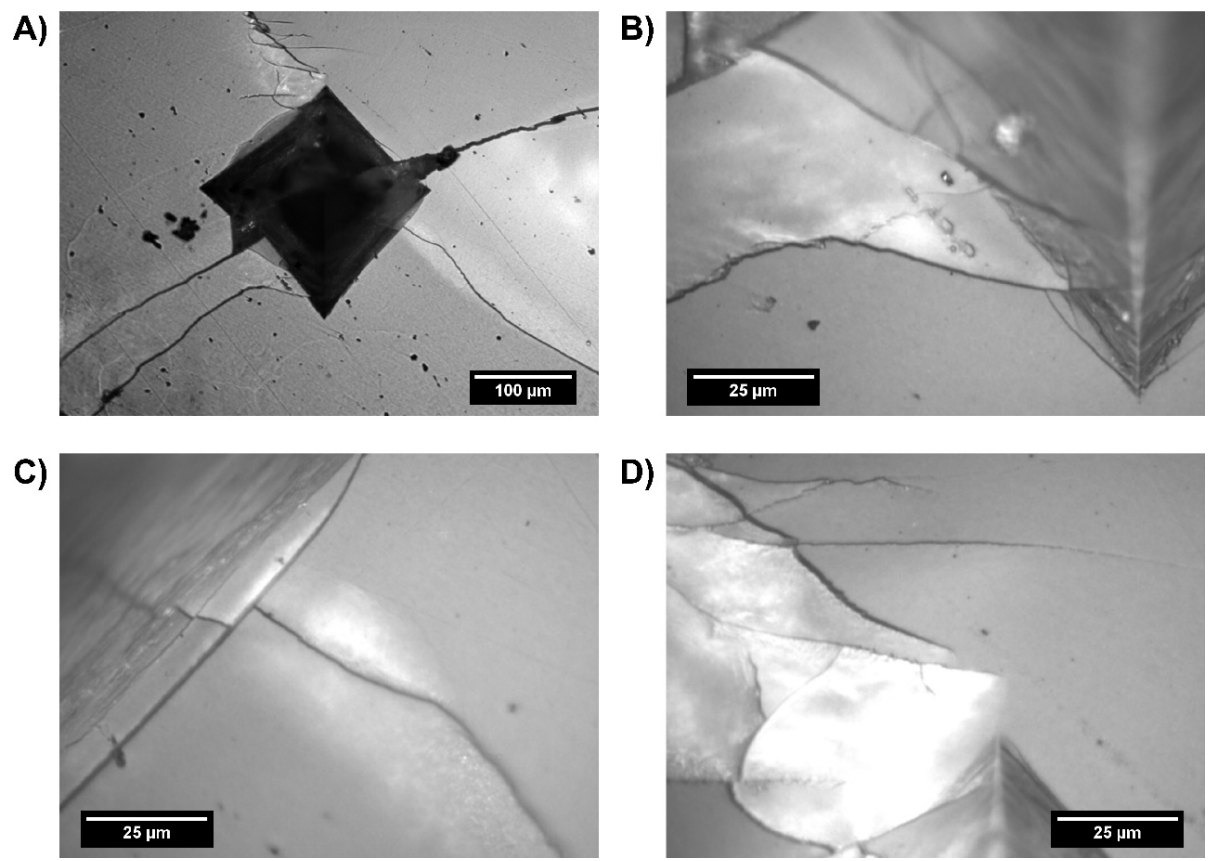
Figure S7. Detail of shear faults on a MOF-808 monolith. A) Overview of the Vickers residual indent HV0.05 (50 gf ~ 0.49 N). B) AFM height topography of a 4×4 μm scan area, highlighted in A). C) AFM height profile along the line highlighted in B), revealing the vertical displacement corresponding to the shear faults.

Figure S8. Vickers HV0.5 (~4.9 N) indent on MIL-68 monolith. Radial cracks propagate from shear faults inside the indent and deflect following low energy paths.
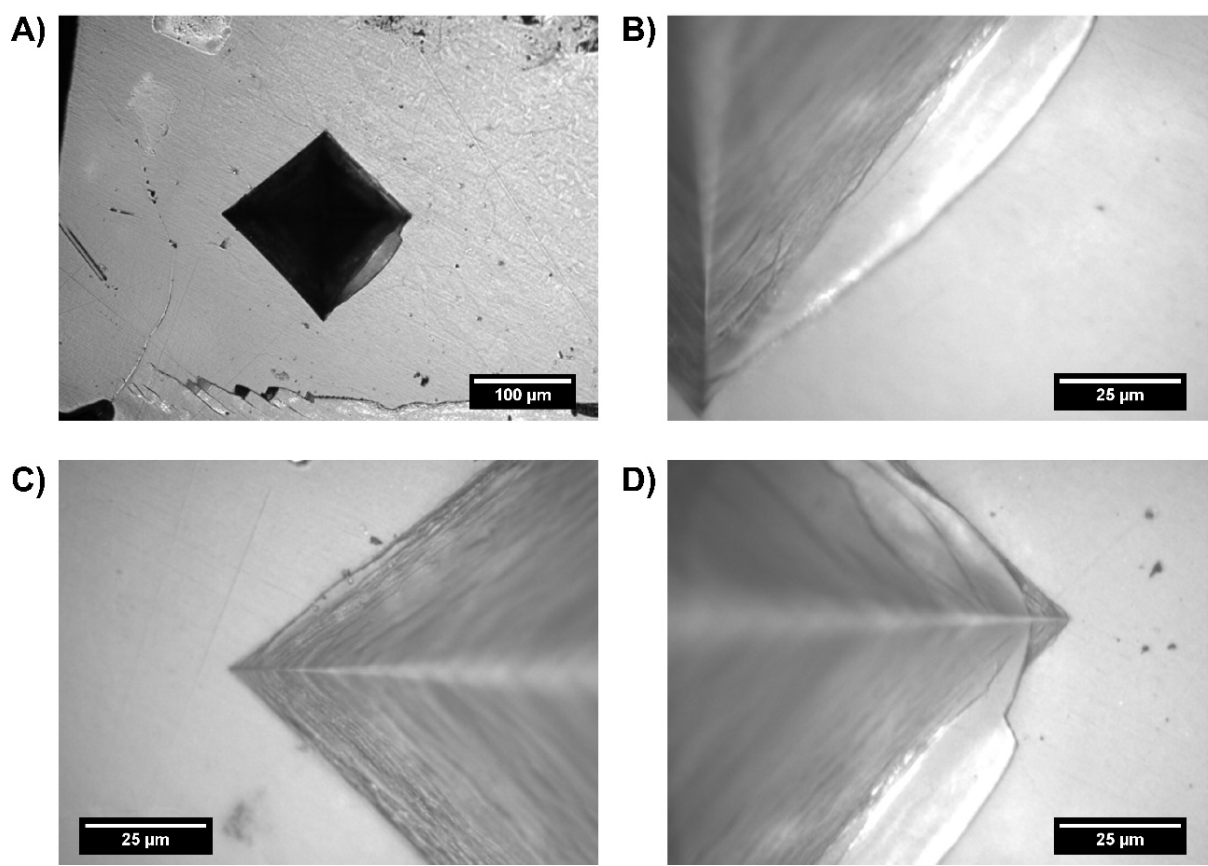
Figure S9. Vickers HV0.5 (~4.9 N) indent on MIL-68 monolith. In this case no radial cracks are induced.
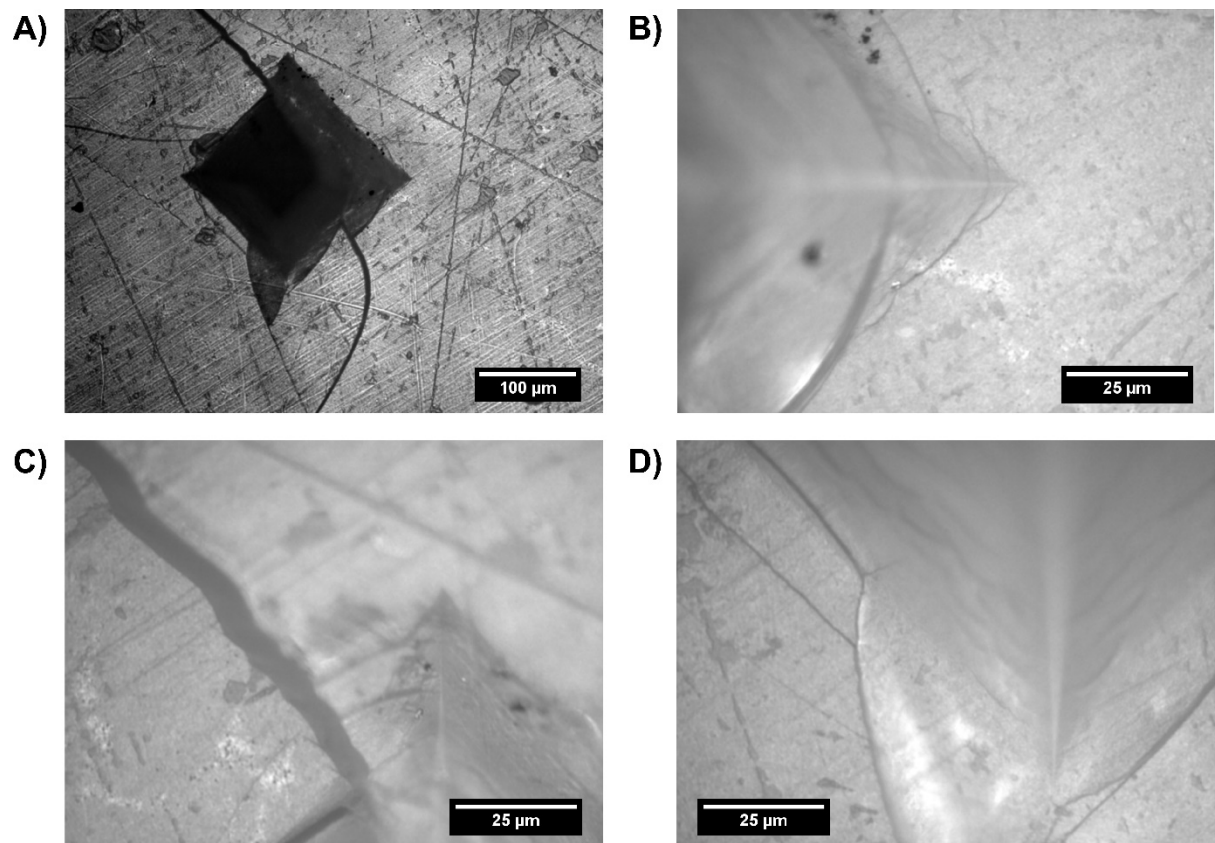
Figure S10. Vickers HV0.3 (~2.9 N) indent on MOF-808 monolith. Radial cracks propagate from shear faults inside the indent and deflect following low energy paths outside the indent.
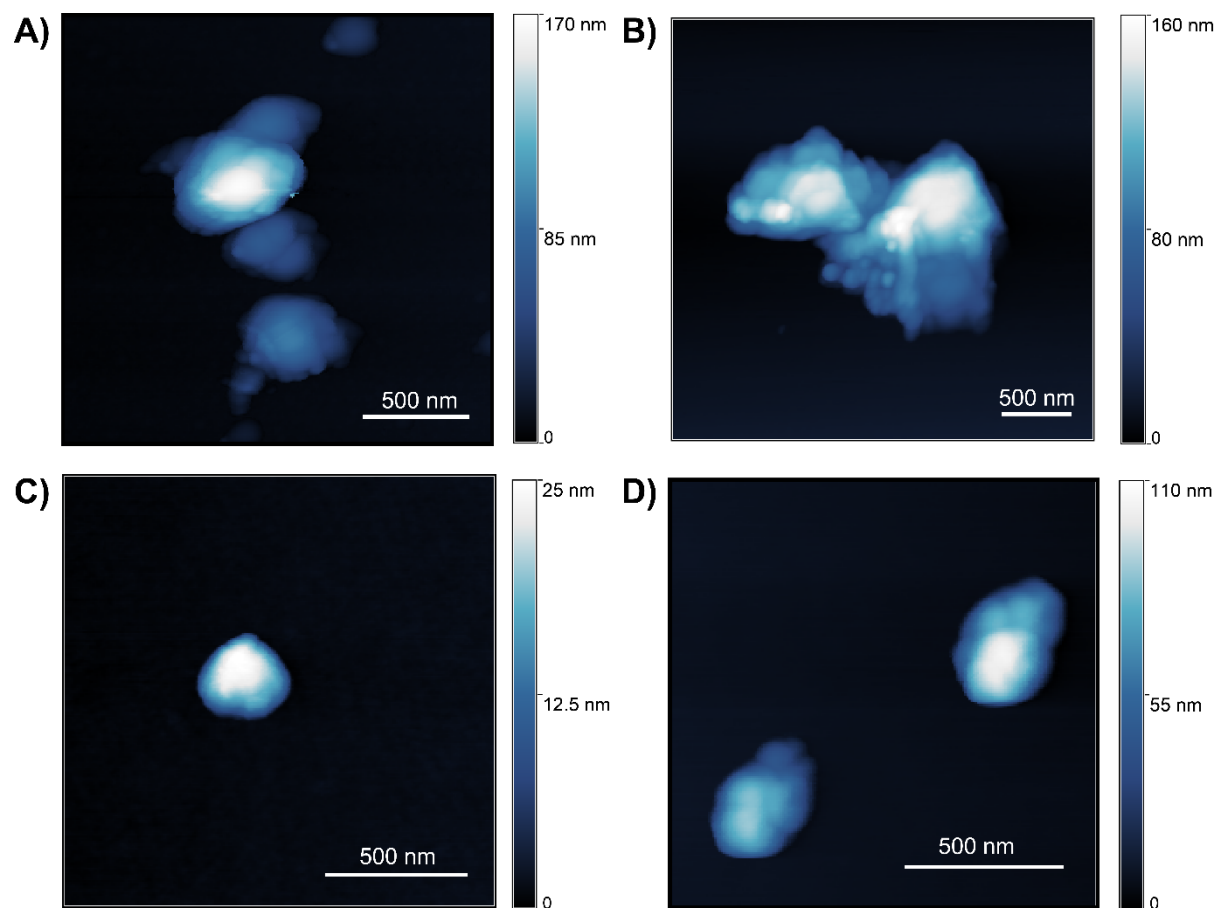
Figure S11. AFM height topography images revealing the morphology and size of A) ZIF-8, B) HKUST-1, C) MIL-68, and D) MOF-808 nanocrystalline aggregates.
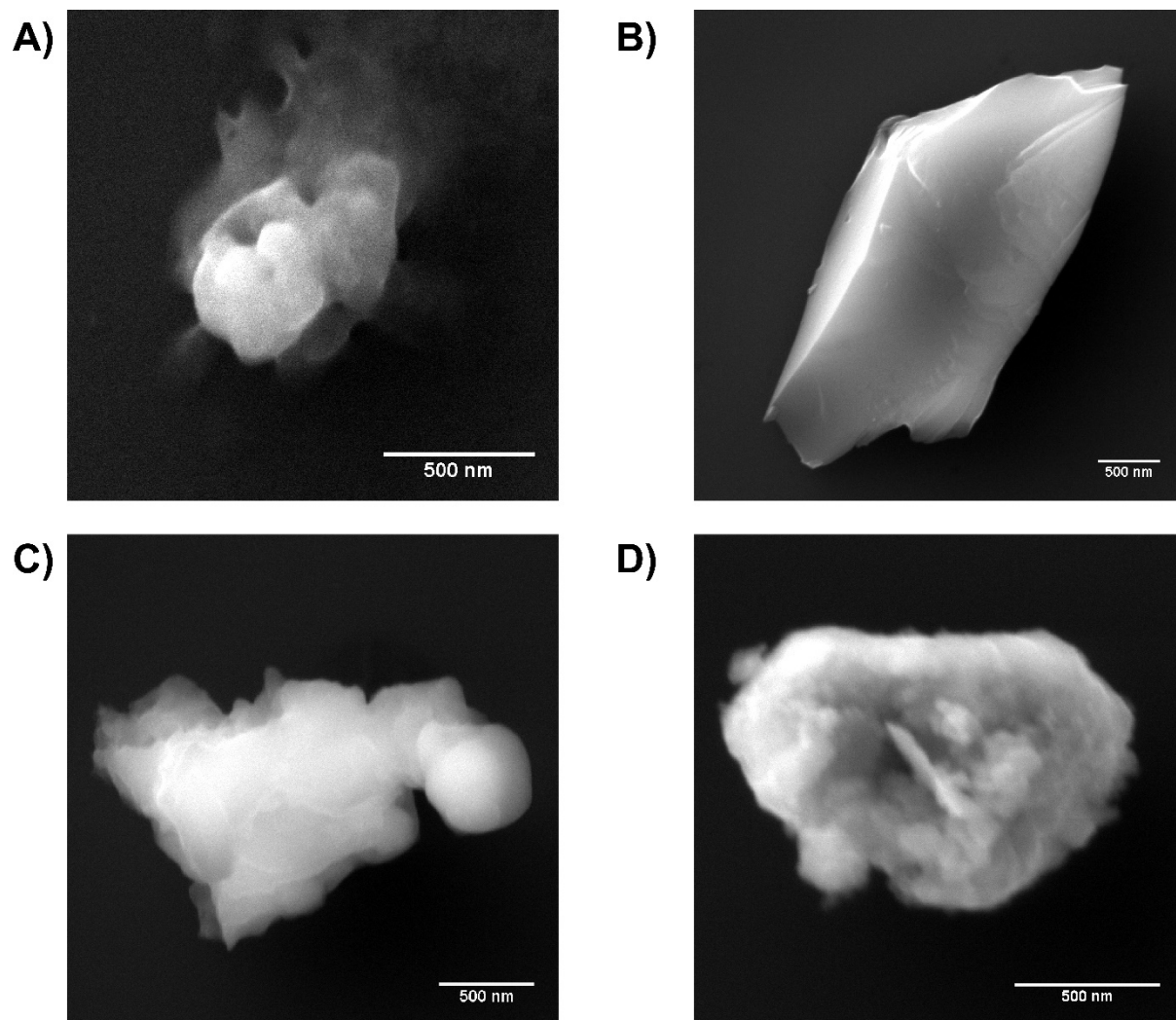
Figure S12. FESEM micrographs revealing the morphology and size of A) ZIF-8, B) HKUST-1, C) MIL-68, and D) MOF-808 nanocrystalline aggregates.
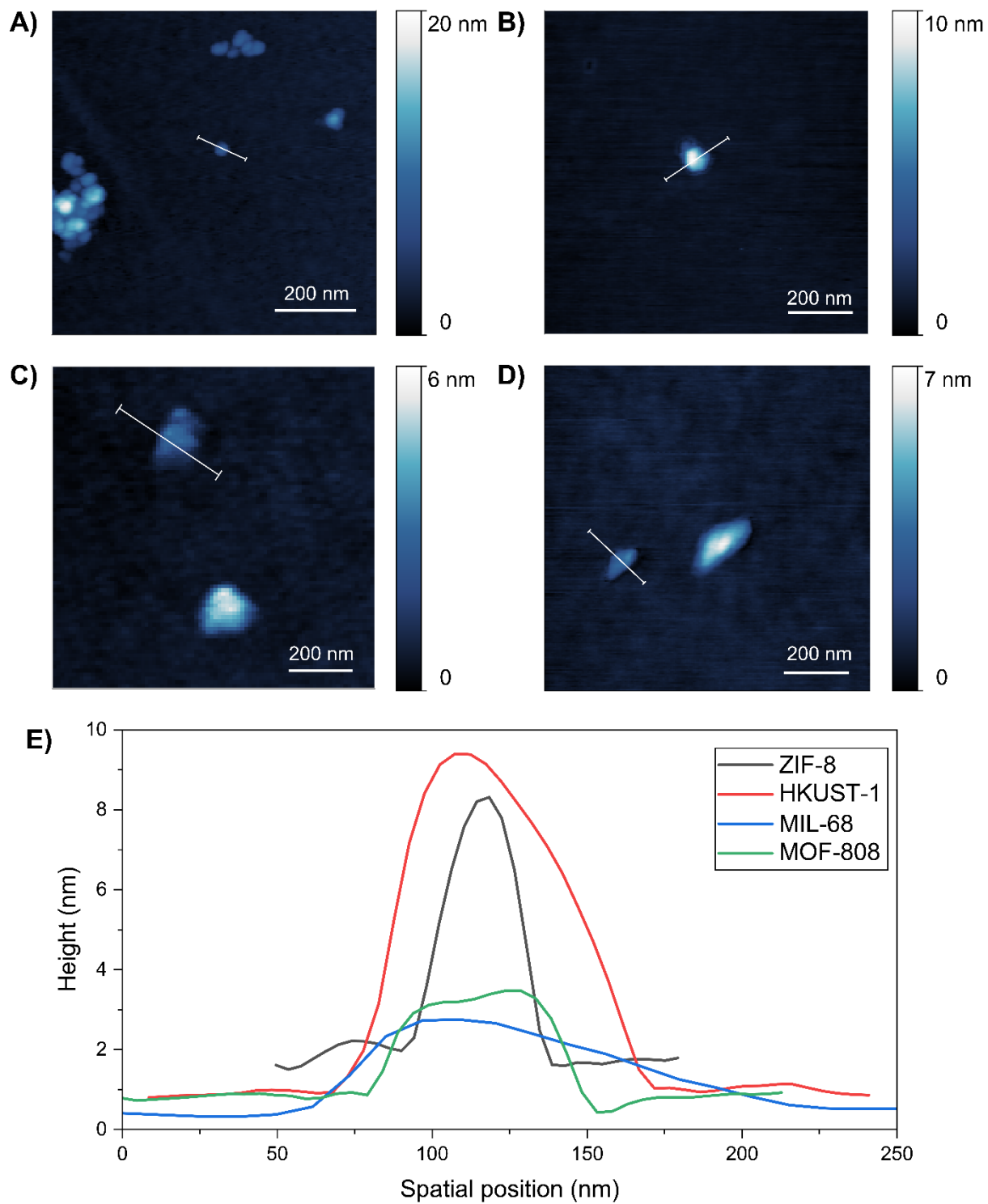
Figure S13. AFM height topography images revealing the nanocrystals morphology and size of A) ZIF-8, B) HKUST-1, C) MIL-68, and D) MOF-808. The corresponding line profiles are plotted in E).
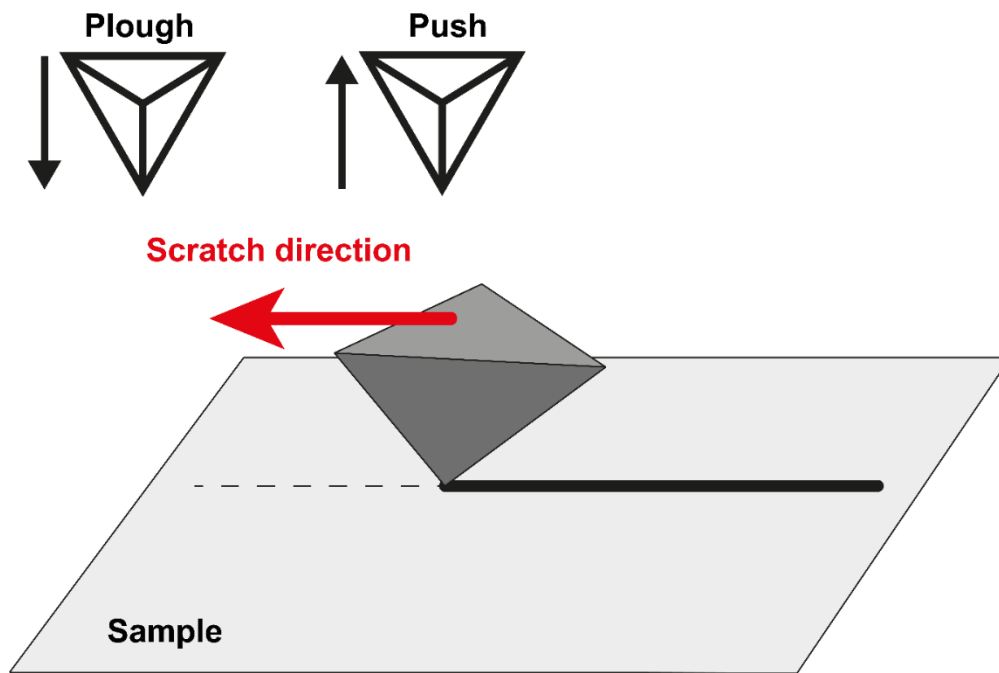
Figure S14. Schematic representation of a scratch test with a Berkovich tip. Since this is a three-sided pyramidal probe, two test modes are possible, depending on which end of the tip is cutting the material: ploughing (sharp end) or pushing (flat end).
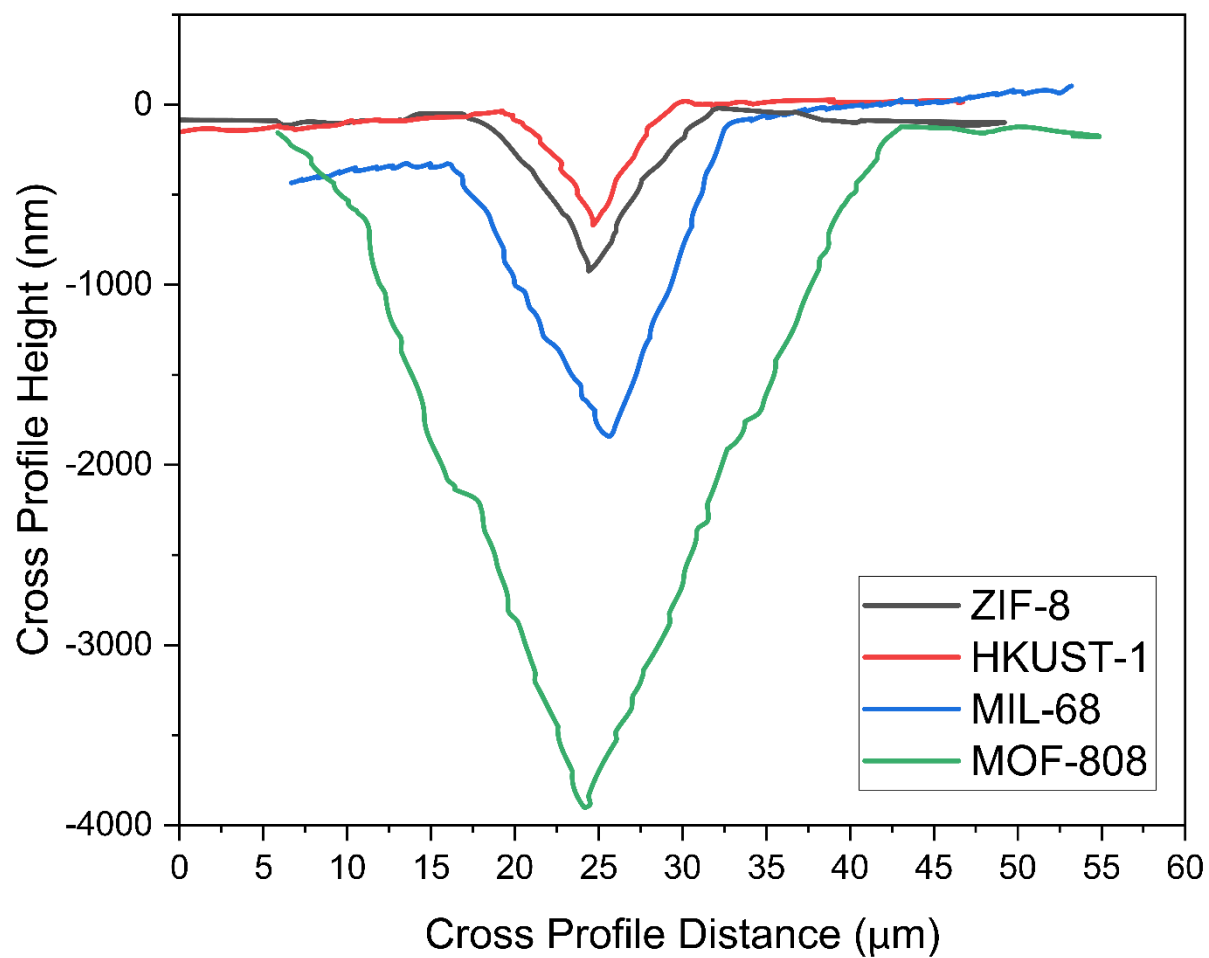
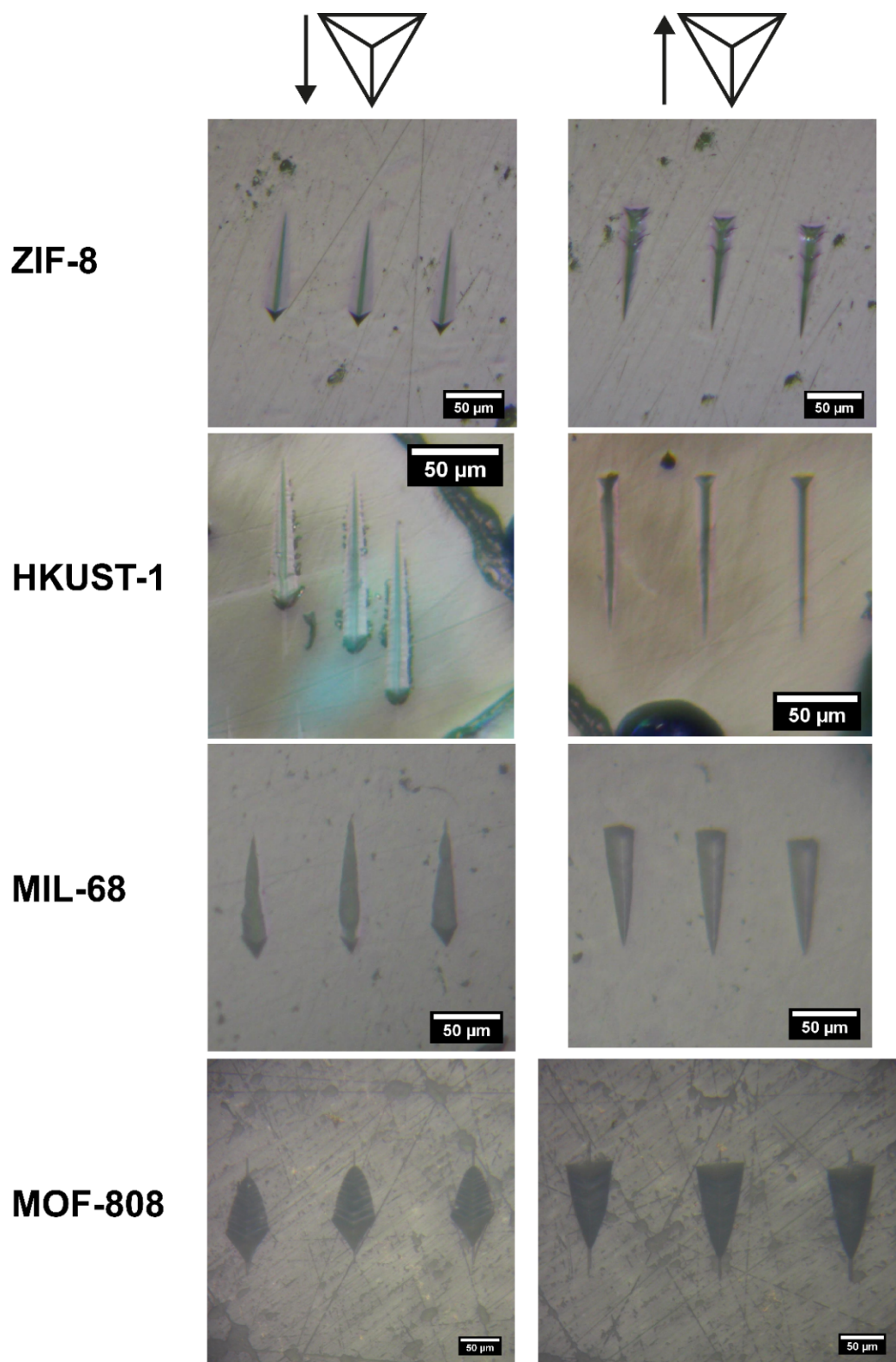**Figure S15.** Representative mid-way cross profiles (load ~25 mN) of scratches in pushing mode on the four monoliths.

Figure S16. Optical micrographs of the scratches on the four monoliths in ploughing mode (left) and pushing mode (right).

SI References

1.   Tricarico, M., and Tan, J.-C. (2022). Mechanical properties and nanostructure of monolithic zeolitic imidazolate frameworks: a nanoindentation, nanospectroscopy, and finite element study. Mater Today Nano *17*, 100166. 10.1016/j.mtnano.2021.100166.
2.   Tan, J.C., Civalleri, B., Lin, C.C., Valenzano, L., Galvelis, R., Chen, P.F., Bennett, T.D., Mellot-Draznieks, C., Zicovich-Wilson, C.M., and Cheetham, A.K. (2012). Exceptionally low shear modulus in a prototypical imidazole-based metal-organic framework. Phys Rev Lett *108*, 095502. 10.1103/PhysRevLett.108.095502.
3.   Ryder, M.R., Civalleri, B., Cinque, G., and Tan, J.-C. (2016). Discovering connections between terahertz vibrations and elasticity underpinning the collective dynamics of the HKUST-1 metal–organic framework. CrystEngComm *18*, 4303-4312. 10.1039/c5ce02347e.
4.   Zhang, Y., Mollick, S., Tricarico, M., Ye, J., Sherman, D.A., and Tan, J.-C. (2022). Turn-On Fluorescence Chemical Sensing through Transformation of Self-Trapped Exciton States at Room Temperature. ACS Sensors *7*, 2338-2344. 10.1021/acssensors.2c00964.